

Performance evaluation of a Semivolatile Aerosol Dichotomous Sampler (SADS) for Exposure Assessment: impact of design issues.

Noredine Rekeb^{1,2}, Benjamin Sutter¹, Emmanuel Belut¹, Evelyne Géhin², Raymond Olsen³

¹INRS, National institute for research and safety, Rue du Morvan, 54519, Vandoeuvre-lès-Nancy, France

²Univ Paris Est Creteil, CERTES, F-94000 Creteil, France

³STAMI, National Institute of Occupational Health, Pb 5330 Majorstuen, N-0304 Oslo, Norway

Correspondence to: Benjamin Sutter (benjamin.sutter@inrs.fr)

Abstract. Aerosols of semivolatile organic compounds (SVOCs) pose significant health risks to workers in various occupational settings. Measuring human exposure to these aerosols requires a separate assessment of the contribution of particles and gases, which is not resolved by existing sampling techniques. Here, we investigate experimentally the performance of the Semivolatile Aerosol Dichotomous Sampler (SADS), proposed in previous studies, for sampling monodisperse liquid particles with aerodynamic diameters between 0.15 and 4.5 μm , corresponding to workplace aerosols. The measured sampling performances are compared to their theoretical counterparts computed by computational fluid dynamics. The effects of leakage rate, repeatability of the assembly, imprecision of the actually machined nozzle diameters and SADS parts misalignment are examined. The SADS assembly is found easily leaky, but consequences on sampling can be overcome when a prior leak test with leakage rate below $4 \text{ Pa}\cdot\text{s}^{-1}$ is passed. Variation of nozzle diameters in the range (-4.5 %, +3.7 %) with respect to nominal values affects marginally (<3 %) aerosol transmission efficiency, but sampling performance is little reproducible during successive SADS assemblies (CV=22.1 % for wall losses). Theoretically unpredicted large (40-46 %) wall losses are measured for particles larger than 2 μm , located mostly (80 %) on the external walls of the collection nozzle. Assembly repeatability issues and simulations of SADS parts misalignment effect by CFD suggest that these undesirable particle deposits are due to the mechanical backlashes of the assembly. Thus, the current design does not guarantee a nozzle misalignment of less than 5 % of the acceleration nozzle diameter, and other important geometric parameters are not further constrained. The promising theoretical sampling performance of the SADS for SVOCs aerosol larger than 1 μm thus falls short of expectations due to mechanical design issues that can be improved before possible field use.

1 Introduction

Semivolatile organic compounds (SVOCs) represent a significant subgroup of volatile organic compounds (VOCs), and their presence in the environment raises concerns due to their association with carcinogenic, mutagenic, and reprotoxic effects (Raffy et al., 2018). One of the defining features of SVOCs is their ability to exist simultaneously in both vapour and particle phases, making their sampling and analysis a complex task. There are varying definitions of SVOCs, with the U.S. Environmental Protection Agency (Technical Overview of Volatile Organic Compounds, 2020) proposing a classification based on boiling points (240-380 °C at atmospheric

36 pressure), while the standard EN 13936 defines them according to their saturation vapour pressure (ranging from
37 0.001 to 100 Pa at room temperature).

38 In occupational settings, SVOCs can be encountered in diverse forms, such as metalworking fluid (MWF) mists,
39 phthalates, pesticides, acrylamides, machining fluids, exhaust gases from diesel engines, and more. Exposure to
40 these pollutants in the workplace can pose health risks to workers, depending on their chemical nature and the
41 extent of exposure. Understanding the health implications requires accurate measurement of both vapour and
42 particle phases, as their behaviour and effects can differ when inhaled in the respiratory system. Notably, the
43 vapour phase's absorption in the respiratory tract is influenced by the SVOC's solubility, while particle deposition
44 in the lung is governed by their aerodynamic diameter (Volckens, 2003). Additionally, direct adsorption of SVOCs
45 on the skin can lead to absorption into the body (Roberts et al., 2009). Thus, it becomes essential to separately
46 quantify the concentrations of each phase that constitutes a semivolatile aerosol.

47 Various sampling techniques have been proposed to evaluate semivolatile aerosol concentrations, including
48 filtration methods, thermodesorption tubes, cyclones, electrostatic precipitators, and multiple "filter + adsorbent"
49 devices. However, these methods often suffer from the issue of evaporation of the particulate phase during
50 sampling, leading to biased measurements. Filtration methods, for instance, have been found to underestimate
51 particle concentrations due to continued evaporation from the filter during sampling (Park et al., 2015; Raynor et
52 al., 2000; Simpson, 2003; Simpson et al., 2000; Volckens et al., 2010). Other techniques that do not instantaneously
53 separate particles and vapour also face the problem of evaporation during sampling (Raynor and Leith, 1999; Leith
54 et al., 2010; Lillienberg et al., 2008; Wlaschitz and Höflinger, 2007; Sutter et al., 2010; Kim and Raynor, 2010a).
55 As of now, no applicable model exists to theoretically calculate the evaporation of a semivolatile aerosol during
56 workplace air sampling, which hampers the use of these techniques.

57 An alternative approach is the Virtual Impactor (VI) principle, inspired by classical inertial impactors with
58 collection plates (Loo and Cork, 1988; Marple and Chien, 1980). The VI is employed for size classification of
59 particles based on their aerodynamic diameter. In 2009, the Semivolatile Aerosol Dichotomous Sampler (SADS),
60 a novel variant of the VI dedicated to SVOCs, was proposed by Kim and Raynor (2009) and raised great hopes
61 for this application. A photography of a SADS prototype is presented in Figure 1.

62 In its original version, the SADS features an inverted flow configuration between the major and minor flows,
63 resulting in 86 % of the total air being directed into the collection nozzle, while the remaining 14 % is suctioned
64 perpendicular to the acceleration nozzle axis (Figure 2). The aerosol is sampled through a 4 mm inlet orifice and
65 accelerated through a convergent shape called the "acceleration nozzle", which narrows to a 0.8 mm orifice
66 diameter. In the separation space, inertial particles are directed into the collection nozzle, while low inertial
67 particles and vapours follow both the major and minor flows. The collection nozzle, located 1.2 mm from the
68 acceleration nozzle, has a diameter of 1.1 mm, and filters and adsorbent beds are placed at each outlet (major and
69 minor flow). The SADS operates at a total sampling flow rate of 2.1 L.min⁻¹, split into 1.8 L.min⁻¹ at the major
70 flow outlet and 0.3 L.min⁻¹ at the minor flow outlet (split ratio of 0.143).

71 The SADS was further optimized numerically and tested both in the laboratory and in the field by its designers
72 (Kim and Raynor, 2010a, b; Kim et al., 2014). The optimized version is characterized essentially by a revised split
73 ratio of 0.1 with a total sampling flow rate of 2 L.min⁻¹ and with a length of the separation space reduced to
74 0.48 mm instead of 1.2 mm. The angle of the acceleration nozzle was also changed from 19° to 45° between the
75 2009 and 2010 versions. Despite these modifications, the overall mechanical design of the SADS has not changed

76 between these two versions. The overall shape of the device is that of a 37 mm cassette, and it is made up of two
77 parts that fit together via a cylindrical bearing surface. The parts are held together by 2 screws. Sealing is ensured
78 by an O-ring between the two parts, pressed together by the two screws.

79 Thus, the work of Kim et al. led to the creation of the SADS concept and revealed its interest in the sampling of
80 semi-volatile aerosols. However, many questions remain before SADS can be considered sufficiently mature for
81 widespread use as a portable sampling device for SVOC aerosols.

82 Firstly, the sampling performance of the device was not evaluated in detail for particles with aerodynamic
83 diameters greater than 1 μm , as the initial device was not designed for this. However, for field use, the evaluation
84 of the performance of the SADS for particles above 1 μm is especially important because workplace SVOCs
85 aerosols showed a presence of particles with diameters up to 10 μm (Cooper et al., 1996; Park et al., 2009). Since
86 the metric of SVOC exposure is mass concentration, and the mass carried by particles increases with the cube of
87 their diameter, sampling errors on the most inertial particles generate biases in exposure measurements that are far
88 more problematic than sampling errors on sub-micron particles. Optimization work by Kim et al. focused on
89 reducing the cut-off diameter of the device around an aerodynamic diameter of 0.7 μm , but the impact on super-
90 micron particle sampling was not assessed. Subsequent tests on real aerosols revealed significant deposits in the
91 device that had not been anticipated by the theoretical study, and the exact origin of these deposits is still unknown
92 (26.5 % of wall losses for an aerosol with MMAD of 2.17 μm in Kim and Raynor (2010b) and separate evaluations
93 by NIOH, Norway and Fraunhofer ITEM that showed similarly high deposition ratios (Olsen et al., 2013)).

94 Secondly, it's important to emphasize the absence of published documentation or feedback regarding the
95 mechanical realization and the necessary operating procedures for obtaining measurements in line with theoretical
96 performance for the SADS. It is well known that the details of mechanical design and manufacture have as much
97 to do with impactor performance as the theoretical design: sealing, nozzle alignment (Loo and Cork, 1988),
98 geometric assembly tolerances - these are all necessary qualities which are the consequence of a suitable
99 mechanical design. So far, the SADS design proposed by Kim et al. has not been studied from these aspects, and
100 it is possible that a more definitive version of the SADS will require a review of its overall mechanical design,
101 without modification of the interior volume, which is perhaps optimal. Summarily, the authors who worked on the
102 SADS have neither published documentation related to these aspects nor investigated them in previously published
103 articles. In particular, it is doubtful whether the device as shown in Kim and Raynor (2010b) is leak-tight, with
104 only two diametrically opposed clamping points. Also, in both versions, the proposed design does not seem to
105 guarantee a precise control of nozzle spacing and alignment during assembly (limited guides and ground seats).

106 Finally, it is not certain that the optimized version proposed in 2010 is really optimal for sampling semi-volatile
107 aerosols encountered at workplaces, for various reasons. Firstly, from a methodological point of view, the
108 optimization carried out is based on a Computational Fluid Dynamics (CFD) model, which does not appear to
109 provide accurate enough results for the optimization approach to be conclusive, as exposed in Belut et al. (2022).
110 This is notably illustrated by significant differences between CFD predictions and measurements, for both the
111 airflow and the aerosol phase (modelled pressure drop on the major flow side is more than twice the measured
112 value for Kim and Raynor (2009), measured and simulated particles separation efficiencies depart by as much as
113 30 % in Kim and Raynor (2009) and by as much as 53 % in Kim and Raynor (2010b), simulations report almost
114 no particle deposition but experimental evaluations found important wall losses: 26.5 % for an aerosol with
115 MMAD of 2.17 μm in Kim and Raynor (2010a) and separate evaluations by NIOH, Norway and Fraunhofer ITEM

116 showing similarly high deposition ratios (Olsen et al., 2013). Secondly, the 2010 version has a much steeper inlet
117 convergent angle (acceleration nozzle) than the 2009 version, which increases the probability of undesirable wall
118 loss for the most inertial aerosols (Belut et al., 2022).

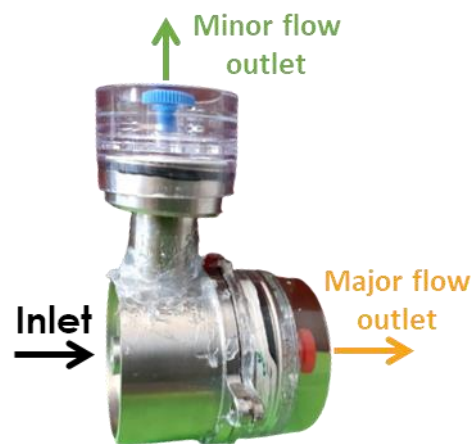
119 In this context, the present article:

- 120 - Conducts an experimental investigation into the size-resolved sampling performances of the SADS on
121 liquid SVOCs particles within an aerodynamic diameter range of 0.15-4.5 μm , i.e., extending beyond
122 previous studies;
- 123 - Identifies practical issues related to the design, manufacturing and operation of the SADS as proposed in
124 Kim and Raynor (2009, 2010b);
- 125 - Investigates the effect of small variations in SADS nozzle diameters due to inevitable random
126 manufacturing uncertainties;
- 127 - Details the localization of wall losses in the device, as mentioned in prior research, and identifies their
128 cause.

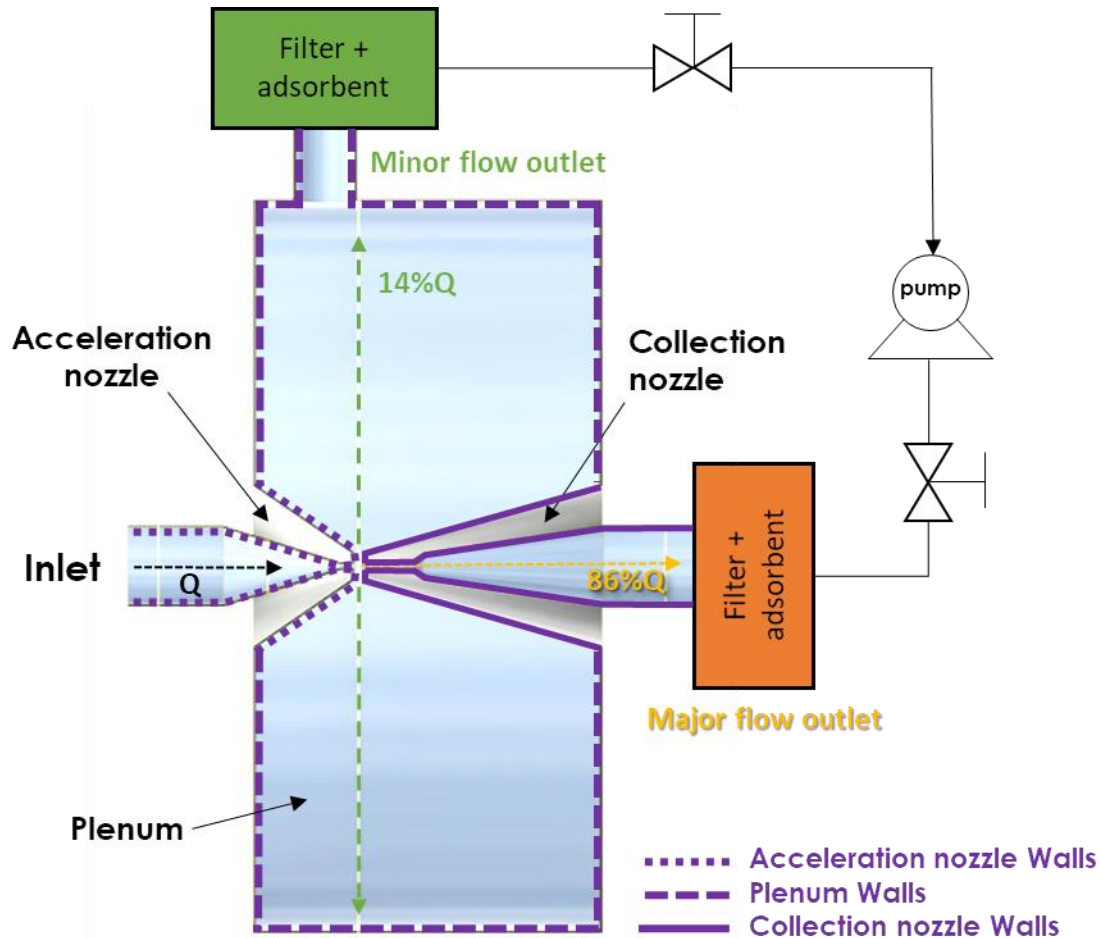
129 In doing so, our aim is to suggest improvement targets for future realization of the SADS, a small step to obtain a
130 device suitable for the dichotomic measurement of particles and vapours composing SVOCs aerosols at
131 workplaces. We shall base our study on the 2009 version of the SADS, because of the smaller cut-off diameter
132 and also considering that the issues related to the overall design of the SADS are common to both versions.

133 To reach our objectives, five 2009 SADS prototypes were constructed and their sampling behaviour was
134 characterized, using monodisperse liquid aerosols of various sizes. After evaluating the leakage resistance of the
135 assembly, and its consequences on wall deposition, the actual sampling performances are compared to their
136 theoretical counterparts computed by Belut et al. (2022). Origin of discrepancies are examined in terms of
137 influence of the actually machined nozzle diameter and of the repeatability of the SADS assembly. An analysis of
138 the distribution of deposits within the SADS is then used to estimate the likely cause of deposits in the device. The
139 results are then discussed to propose improvement targets for the realization of the SADS, in terms of design and
140 assembly.

141 Where necessary, CFD simulation results are used to support the observations. The approach of Belut et al. (2022)
142 is then used for this purpose, including systematic calculation verification steps.



143
144 **Figure 1 : Photography of a SADS with schematic airflows directions.**



146

147 Figure 2: Schematic diagram of the Semi-volatile Aerosol Dichotomous Sampler (SADS). The diagram illustrates
 148 the positioning of the acceleration and collection nozzles, the division of the inlet airflow into a major (86% of the
 149 inlet flow) and a minor flow outlet (14% of the inlet flow). Each outlet is equipped with a filter and adsorbent for
 150 effective aerosol sampling. The different types of walls, used to determine the mass of particles collected on, are
 151 depicted by various dashed lines: Acceleration nozzle Walls, Plenum Walls, Collection nozzle Walls.

152 2 Principle of the particle-vapour dichotomous sampling in the SADS and definitions

153 The SADS is derived from the VI principle with an inverted split ratio between the major flow and the minor flow.
 154 The intended behaviour is as follows: the mixture of air, SVOCs vapours and SVOCs aerosol particles is drawn
 155 into the device through its inlet (Figure 2). This mixture is first accelerated by a convergent nozzle and reaches the
 156 separation gap of the device. In the separation gap, a small fraction of the flow is deflected laterally and directed
 157 to a first outlet, while a large fraction continues forward through a divergent collection nozzle. Because of their
 158 inertia, the particles should preferentially follow the main flow, while the concentration of the vapours remains
 159 unaffected by the separation of the flow. With ideal sizing, the minor flow is then free of particles, allowing the
 160 concentration of the vapor phase of the sampled SVOCs to be measured. Subtracting this vapor contribution from
 161 the mass of SVOCs collected with the main stream then allows the concentration of SVOC aerosol particles only
 162 to be retrieved. With an ideal design, the SADS then allows dichotomous analysis of airborne SVOCs.

163

164 For a given aerodynamic diameter of particles d_{ae} , the particles transmission efficiency $\eta_p(d_{ae})$ to the particle
165 major flow outlet is defined as the ratio of particle mass collected at the major flow outlet to the total particulate
166 sampled mass of particles with the same diameter (Eq. 1):

$$167 \quad \eta_p(d_{ae}) = \frac{m_{major}(d_{ae})}{m_{inlet}(d_{ae})} \quad (1)$$

168 Similarly, $\eta_v(d_{ae})$ is the particles transmission ratio to the particle minor flow outlet, defined by the ratio of the
169 particle mass collected at the minor flow outlet to the total particulate sampled mass (Eq. 2), for a given particle
170 size.

$$171 \quad \eta_v(d_{ae}) = \frac{m_{minor}(d_{ae})}{m_{inlet}(d_{ae})} \quad (2)$$

172 Finally, we defined a particles deposition ratio $\eta_d(d_{ae})$ that correspond to the ratio of the mass deposited on the
173 inner wall of the SADS to the total particulate sampled mass, for a given particle size (Eq. 3):

$$174 \quad \eta_d(d_{ae}) = \frac{m_{dep}(d_{ae})}{m_{inlet}(d_{ae})} \quad (3)$$

175 In ideal working conditions of the SADS as a gas-particle separator, we expect η_d and η_v to be zero while $\eta_p=1$.
176 The details of the device's geometric dimensions and the choice of minor and major flow rates determine the
177 device's theoretical separation performance (Loo and Cork, 1988; Marple and Chien, 1980). In the present article,
178 these choices are assumed to be theoretically optimal, and we study only the effects of certain design and
179 manufacturing details on the device's ability to actually achieve its theoretical performance. Hence, minor and
180 major flows are set constant at their theoretical optimum as specified.

181

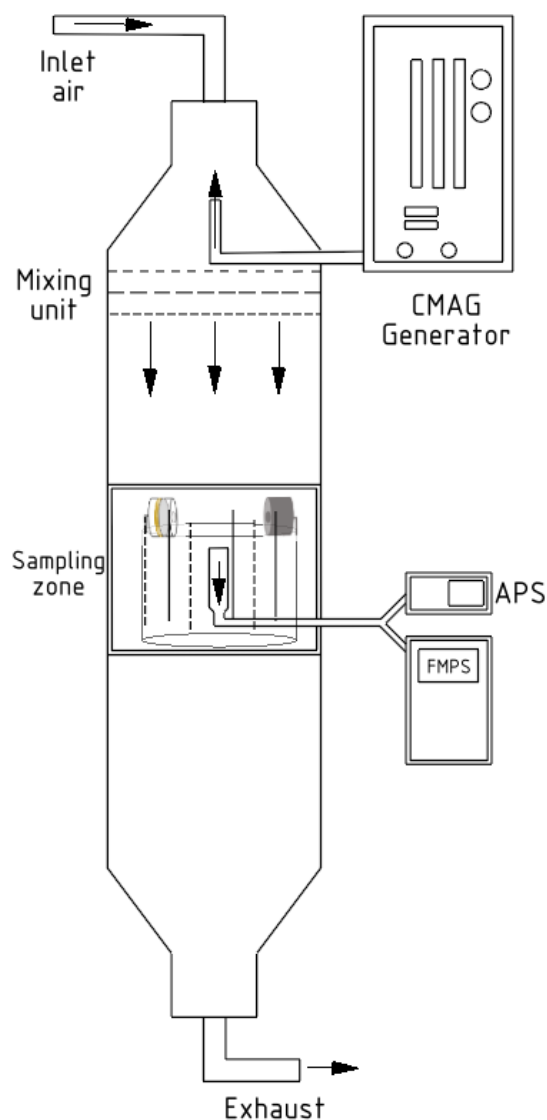
182 In these conditions, the theoretical performances of the SADS in terms of η_p , η_v and η_d has been extensively
183 studied numerically by (Belut et al., 2022), their work highlighting the main factors influencing the
184 representativeness of the CFD modelling of similar devices. In described operating conditions, they indicate that
185 $\eta_v = 0$ and $\eta_p > 98\%$ for d_{ae} in $[0.9 - 20] \mu\text{m}$ (perfect separation). We may introduce a d_{50} cut-off diameter as
186 the aerodynamic diameter of particles below which η_v is equal to half its maximum value of 0.143 (corresponding
187 to no separation, in this case η_v equals the gas split ratio). Results from (Belut et al., 2022) indicate that the
188 theoretical d_{50} of the SADS is $0.44 \mu\text{m}$, i.e. much smaller than most of SVOCs aerosol diameters at the workplace.
189 The SADS is hence in theory perfectly suitable for field use, where most of SVOCs aerosol diameters are above
190 (Cooper et al., 1996; Park et al., 2009). However, these performances are theoretical, whence the necessity of
191 finding the conditions under which this is valid in actual realization of the SADS.

192 **3 Material and methods**

193 **3.1 Aerosol generation**

194 To assess the performance of the Semivolatile Aerosol Dichotomous Sampler (SADS), aerosols were generated
195 using a specialized equipment called the Bench for Organic Aerosol (BOA), as depicted in Figure 3. The BOA is
196 a vertical wind tunnel designed to operate with controlled airflow velocities ranging from 0.1 to $0.5 \text{ m}\cdot\text{s}^{-1}$ and
197 humidity levels between 10 to 90% RH. Aerosols were introduced counter current at the head of the tunnel to
198 ensure thorough mixing with the airflow. To achieve spatially homogeneous mixtures at the sampling zone, the

199 air/aerosol mixture passed through a series of diaphragms with different meshes. The SADS prototypes, along
200 with an isokinetic nozzle connected to online instrument measurements, were placed on a crown support in the
201 sampling zone.



202
203

Figure 3: Schematic drawing of the Bench for Organic Aerosol (BOA) generation device.

204 To maintain consistent experimental conditions, room temperature was set to 21 °C, atmospheric pressure was
205 measured at 1018 ± 10 hPa, relative humidity was regulated at 20 %RH, and airflow velocity was fixed at
206 $0.2 \text{ m}\cdot\text{s}^{-1}$. The airflow inside the tunnel was considered isothermal, incompressible, and turbulent, with a Reynolds
207 number based on the tunnel size of approximately 4×10^3 .

208 The BOA was carefully calibrated to meet the requirements of the standard NF EN 13205-2:2014. Spatial
209 homogeneity of velocities in the sampling section was confirmed, with the standard deviation below 1 % over the
210 entire sampling zone. Similarly, the spatial homogeneity of particle concentration demonstrated standard deviation
211 values below 10 %.

212 3.2 Aerosol generator

213 To produce aerosols for testing the SADS prototypes, a specialized Condensation Monodisperse Aerosol Generator
214 (CMAG - TSI 3475) based on Sinclair-La Mer principle (Sinclair and La Mer, 1949) was employed. This specific
215 generator condenses heated vapours of diethyhexyl sebacate (DEHS) homogeneously on thin particles of sodium
216 chloride, referred to as nuclei, to form monodispersed liquid particles. The size of these particles ranges from 1 to
217 8 μm , depending on the selected generation conditions. Originally designed for use with diethyhexyl sebacate
218 (DEHS) and NaCl, the CMAG was modified to accommodate the use of glycerol and fluorescein (Steiner et al.,
219 2017). This modification was necessary as DEHS is not water-soluble, making the analysis of particles collected
220 on filters or internal walls of the sampler challenging and less sensitive. By replacing DEHS with glycerol and
221 NaCl with fluorescein, water-soluble droplets were generated, and fluorescein could be quantified at a very low
222 concentration (i.e., $\text{LoQ} < 1 \text{ ng.L}^{-1}$ within water extract).

223 The aerosol production process within the CMAG initiates with the nebulization of a water solution, specifically
224 composed of 0.8 g.L^{-1} fluorescein and 5 g.L^{-1} sodium hydroxide in pure water, within an atomizer. This step is
225 succeeded by the drying of the droplets in a diffusion dryer. Following the diffusion dryer, small nuclei, constituted
226 of a blend of fluorescein and sodium hydroxide, were generated. These nuclei, serving as condensation nuclei,
227 exhibited sizes ranging from 10 to 100 nm. These nuclei were then exposed to a saturated vapour of glycerol
228 downstream of the saturator. The resulting mixture of glycerol vapour and nuclei was directed to a re-heater and
229 subsequently cooled down in a condensation chimney to produce the monodispersed aerosol.

230 It is important to note that the size of the generated particles could be adjusted by modifying the temperature of
231 the saturator or the number concentration of nuclei. For this study, aerosols with mass median aerodynamic
232 diameters (MMAD) of circa 0.15, 2, 3, and $4.5 \mu\text{m}$ were produced and used for the experiments.

233 3.3 Aerosol characterization

234 Characteristics of the generated aerosols were measured continuously during the generation process. Aerodynamic
235 particle sizes and geometric standard deviations (GSD) were measured using a TSI Aerodynamic Particle Sizer
236 (APS 3321) associated with an aerosol diluter (TSI 3302 A) for particles ranging from 0.5 to $20 \mu\text{m}$. For particles
237 ranging from 0.056 to $0.560 \mu\text{m}$, a TSI Fast Mobility Spectrometer (FMPS – 3091) was used. The FMPS apparatus
238 measures a mobility diameter that was converted in this study in an aerodynamic diameter using the following
239 equations, considering that all particles generated during this study were spherical:

$$240 \quad d_{ae} = d_m \left(\frac{Cu(d_m) \rho_p}{Cu(d_{ae}) \rho_0} \right)^{1/2} \quad (4)$$

241 Where d_m is the particle mobility diameter, d_{ae} the aerodynamic diameter, Cu the Cunningham correction factor
242 calculated with the appropriate diameter, ρ_0 the reference density (1000 kg.m^{-3}) and ρ_p and the real density of the
243 particle (kg.m^{-3}).

244 The particle density exhibits variability between nuclei and condensed glycerol particles. Based on the initial
245 composition of the fluorescein solution utilized for generating nuclei, the density of the nuclei was determined to
246 be 1720 kg.m^{-3} after total desiccation. In contrast, the density of the condensed particles is approximated to the
247 density of pure glycerol, given the negligible mass of the nuclei compared to the mass of glycerol that condenses
248 on them. Consequently, particles with diameters of $2 \mu\text{m}$ and above are considered to possess a density of
249 approximately 1260 kg.m^{-3} .

250 To further enhance the relevance of this study, the physical diameter of the particles is approximated by the
 251 measured aerodynamic diameter, considering the spherical nature of the particles. This approximation facilitates
 252 the conversion of the number-based particle size distribution into a mass-based particle size distribution, a
 253 parameter of greater significance for our research objectives. Following the conversion from a number-based to a
 254 mass-based particle size distribution, we proceeded to calculate the mass median aerodynamic diameter (MMAD).
 255 This parameter serves as a valuable metric, providing a comprehensive characterization of the aerosol particles in
 256 our investigation.

257 The measurement of aerosol characteristic by APS and FMPS apparatus allow modulating the particle diameter
 258 produced by the CMAG and verifying the stability of the aerosol concentration during the experiment. Averages
 259 are shown in Table 1. Note that the aerosol with a MMAD of 0.16 μm exhibited a high GSD of 1.56, which does
 260 not meet the monodisperse criteria with a GSD < 1.2. Specifically for this aerosol, the particles measured were
 261 actually nuclei generated by removing the glycerol from the CMAG. Consequently, without glycerol condensation
 262 on their surfaces, their diameters could not be homogenized. In summary, we typically measured the particle size
 263 distribution of nuclei generated before condensing glycerol on them to produce micron-monodispersed particles

264 **Table 1: Averaged particle size distributions of the test aerosols (N=3 \pm SD).**

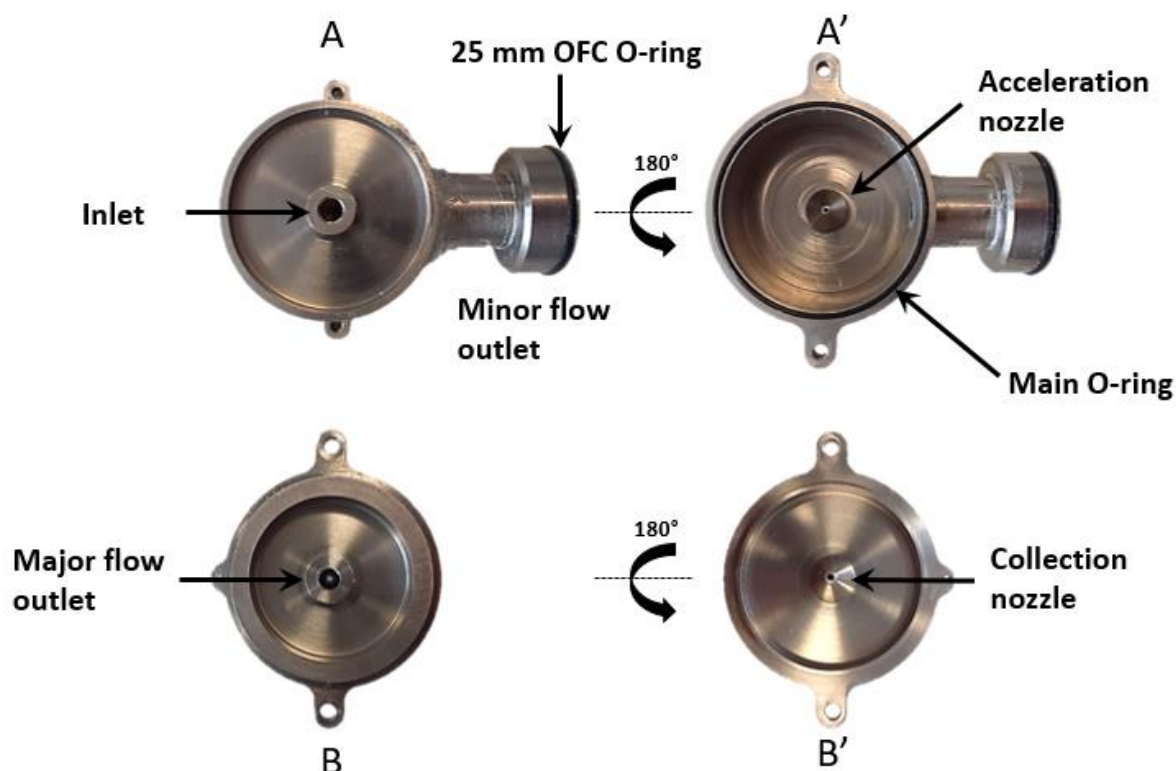
Aerosol reference diameter (μm)	MMAD \pm SD (μm)	GSD \pm SD
0.15	0.16 \pm 0.05	1.56 \pm 0.02
2	2.04 \pm 0.15	1.16 \pm 0.03
3	3.17 \pm 0.21	1.14 \pm 0.01
4.5	4.70 \pm 0.12	1.10 \pm 0.02

265 The stability of aerosol concentration in the sampling zone was verified, with a mass concentration deviation
 266 below 6 % across experiments.

267 3.4 SADS prototypes

268 The STAMI, Norway, had five titanium SADS Kim & Raynor (2009) prototypes. Photographs of the SADS
 269 prototype components are presented in Figure 4, illustrating the acceleration nozzle and the collection nozzle,
 270 along with the connection of a cassette to the SADS sampler. The SADS prototypes investigated in this study were
 271 manufactured by a precision mechanics workshop, resulting in slight deviations in their nozzle diameters compared
 272 to the reference dimensions proposed by Kim & Raynor (2009). These deviations were attributed to the inherent
 273 tolerance of the manufacturing process. Specifically, one of the prototypes (SADS R) exhibited nozzle diameters
 274 identical to those of the 2009 version, serving as the reference case for comparisons. The remaining prototypes
 275 (SADS 1, SADS 2, SADS 3, and SADS 4) showed minor differences in their nozzle diameters relative to the
 276 reference, as detailed in

277 Table 2. The deviations, both absolute and relative, are provided for both the acceleration and collection nozzles.
 278 These dimensions were measured using scanning electron microscopy (SEM) for accuracy. The maximum
 279 deviation of nozzle diameter with respect to the reference dimensions of SADS R (Kim and Raynor (2009)
 280 dimensions) was +0.03 mm (+3.7 %) for the acceleration nozzle and -0.05 mm (-4.5 %) for the collection nozzle.



281
 282 **Figure 4: Photographs of the SADS prototype, consisting of two main components - the acceleration nozzle (A') and**
 283 **the collection nozzle (B'). The upper left photo (A) shows the inlet side of the acceleration nozzle, while the lower left**
 284 **photo (B) displays the outlet side of the collection nozzle. On the outlet side of the collection nozzle (B), a 37 mm**
 285 **cassette is easily connected to the SADS sampler.**

286
 287 **Table 2: Nozzles diameters measured by SEM.**

SADS name	Acceleration nozzle [mm] <i>(absolute difference with reference / relative difference with reference)</i>	Collection nozzle [mm] <i>(absolute difference with reference / relative difference with reference)</i>	Ratio Collection nozzle / Acceleration nozzle
SADS 1	0.83 <i>(+0.03 / 3.7 %)</i>	1.05 <i>(-0.05 / -4.5 %)</i>	1.27
SADS 2	0.82 <i>(+0.02 / 2.5 %)</i>	1.06 <i>(-0.04 / -3.6 %)</i>	1.29
SADS 3	0.798 <i>(-0.002 / 0.3 %)</i>	1.11 <i>(+0.01 / + 0.9 %)</i>	1.39
SADS 4	0.818 <i>(+0.018 / 2.2 %)</i>	1.11 <i>(+0.01 / + 0.9 %)</i>	1.36
SADS R	0.8 <i>(+0.00 / 0 %)</i>	1.10 <i>(+0.00 / 0 %)</i>	1.38

288 **3.5 SADS sampling procedure**

289 The performance evaluation of the five SADS prototypes was conducted simultaneously in the sampling zone of
 290 the Bench for Organic Aerosol (BOA) (Figure 3). Prior to testing, each prototype was meticulously cleaned using
 291 ethanol and pure water. The samplers were equipped with Whatman Quartz Microfiber Filters (QMA) placed into
 292 37 mm and 25 mm Open Face Cassettes (OFC) and connected at the major outlet and the minor outlet (Figure 2),
 293 respectively. The flow rates at the major flow outlet (1.8 L.min⁻¹) and the minor flow outlet (0.3 L.min⁻¹),

294 corresponding to a total inlet flow rate of 2.1 L.min⁻¹, were precisely controlled using flow meters (Gilian
295 Gilibrator-2).

296 **3.6 Fluorescence analysis**

297 After each generation test, the sampling procedure for fluorescence analysis was carried out. The Whatman Quartz
298 Microfiber Filters (QMA) contained in the 37 mm and 25 mm Open Face Cassettes (OFC) were extracted
299 separately and analysed for fluorescence content. Each filter in the CFC and OFC was inserted into independent
300 vials. A volume of 2 to 8 mL of the extraction solution, consisting of ultrapure water with a concentration of 5 g.L⁻¹
301 of NaOH, was added to the vial to dissolve the collected droplets of glycerol and their fluorescein/sodium
302 hydroxide nuclei. The walls of the CFC were also washed with the extraction solution (pure water basified with
303 5 g.L⁻¹ of NaOH), and the resulting volume was combined with the one in the vial containing the CFC filter. After
304 20 minutes of mechanical shaking, the extracts were filtered through a PTFE syringe filter with a pore size of about
305 0.2 µm to prevent any disruption of the fluorescence measurement.

306 Wall deposition inside the SADS was determined by using 2 mL of the extraction solution to wash each wall of
307 the SADS separately. Three different extracts were obtained: one from the acceleration nozzle wall (carried particle
308 mass m_{dep_a}), one from the collection nozzle wall (carried particle mass m_{dep_c}), and one from the plenum wall
309 (carried particle mass m_{dep_p}), (Figure 2).

310 The extracts were then analysed for fluorescence using a portable ESElog Fluorescence Detector (Qiagen,
311 Germany), with an excitation wavelength of 485 nm and an emission wavelength of 520 nm. The linear range of
312 the ESElog Fluorescence Detector defined the lower (LLOQ) and upper (ULOQ) limits of quantification, which
313 covered the concentrations encountered in this work (LLOQ = 0.33 ng.L⁻¹, ULOQ = 4×10⁴ ng.L⁻¹).

314 For each tested aerosol aerodynamic diameter d_a , the total sampled mass m_{inlet} is evaluated as the sum of sampled
315 masses:

$$316 \quad m_{inlet} = m_{dep_a} + m_{dep_c} + m_{dep_p} + m_{major} + m_{minor} \quad (5)$$

317 and the fractional deposition ratio $\eta_d(d_{ae})$ is computed as:

$$318 \quad \eta_d(d_{ae}) = (m_{dep_a} + m_{dep_c} + m_{dep_p}) / m_{inlet} \quad (6)$$

319 and local deposition ratios at the acceleration nozzle (η_{d_a}), collection nozzle (η_{d_c}) and in the plenum (η_{d_p}) are
320 respectively computed from:

$$321 \quad \eta_{d_a} = m_{dep_a} / m_{inlet} \quad (7)$$

$$322 \quad \eta_{d_c} = m_{dep_c} / m_{inlet} \quad (8)$$

$$323 \quad \eta_{d_p} = m_{dep_p} / m_{inlet} \quad (9)$$

$$324 \quad \text{so that } \eta_d = \eta_{d_a} + \eta_{d_c} + \eta_{d_p} \quad (10)$$

325 Because monodispersed aerosols are used, the masses evoked in this paragraph are all linearly related to the amount
326 of fluorescent dye that they carry. Hence, deposition ratios are directly computed from the measured masses of
327 fluorescent dye.

328 **3.7 Mass balance verification**

329 A mass balance verification step was adopted to verify that the protocol allowed recovering all particles sampled
330 by the SADS. The SADS prototypes and 37-mm Closed Face Cassettes (CFCs) equipped with Whatman Quartz

331 Microfiber Filters (QMA) were arranged alternately on the crown support (Figure 5). The 37-mm CFCs equipped
 332 with Whatman Quartz Microfiber Filters (QMA) served as reference samplers, enabling the determination of the
 333 total mass of particles collected on the filter and walls of the CFC, in comparison to the particle mass measured
 334 by the SADS prototypes.

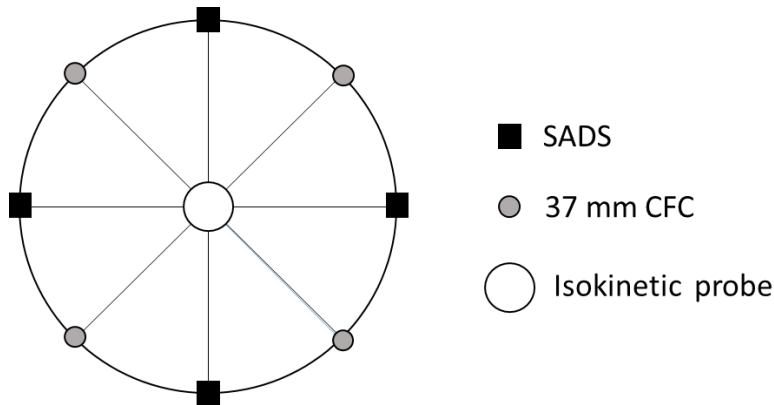
335 All SADS and 37-mm CFCs presented a standardized 4 mm aerosol-sampling orifice and operated at the same
 336 sampling flow rate of 2.1 L.min⁻¹. This standardization ensured that the total mass collected inside the 37-mm
 337 CFCs corresponded to m_{inlet} , the total mass sampled by the SADS, which includes the contribution of both the
 338 Open Face Cassettes (OFC) placed at the minor and major flow outlets and the wall deposits. By comparing m_{inlet}^i ,
 339 the total particle mass measured by the SADS i , with the mean reference mass measured by the 37-mm CFCs
 340 ($\overline{m_{CFC}}$), we introduce the mass balance ratio of SADS i as:

$$341 \quad Mb_{SADS}^i = m_{inlet}^i / \overline{m_{CFC}} \quad (11)$$

342

343 This mass balance makes it possible to assess the overall efficiency of the protocol used to measure the distribution
 344 of particles collected by SADS, between deposits and major and minor outlets.

345 Additionally, the use of the 37-mm CFCs allows assessing the spatial homogeneity of the aerosol distribution
 346 within the sampling zone. No significant spatial variation was observed across different positions of the CFCs (CV
 347 < 5 %). With this assurance of spatial homogeneity, the individual SADS mass balance (Mb_{SADS}) was calculated
 348 using equation 5 for each of the SADS prototypes.



349

350 **Figure 5: Schematic representation of the positions of the samplers on the crown support.**

351 **3.8 Leak evaluation**

352 Any form of leakage is known to compromise the sampling performances of aerosol samplers such as SADS, by
 353 disrupting the airflow and path lines within the nozzles and separation zone. Experimental tests were carried out
 354 to examine the leakage resistance of the proposed SADS assembly, to observe the effects of leaks and to determine
 355 an acceptable leakage limit for the SADS.

356 As the SADS operates under depression, a leakage test was performed using a digital pressure calibrator (DPC -
 357 FSM AG) set to a depression of -4000 Pa, equivalent to the operating pressure of the system. Following a
 358 stabilization period, the DPC's internal pump was deactivated, and the pressure was continuously measured to
 359 determine the leakage rate (LR) in Pa.s⁻¹ (Eq. $LR = \frac{|P_0 - P_f|}{\Delta t}$) (12). Three levels of air tightness were defined: low,
 360 medium, and high, corresponding to LR values of $LR \geq 13 \text{ Pa.s}^{-1}$, $4 \text{ Pa.s}^{-1} \leq LR < 13 \text{ Pa.s}^{-1}$, and $LR < 4 \text{ Pa.s}^{-1}$,
 361 respectively.

362 $LR = \frac{|P_0 - P_f|}{\Delta t}$ (12)

363 Where P_0 and P_f represent the pressures at $t = 0$ s and at the final time, respectively, and Δt is the duration of the
364 leak test.

365 **3.9 Supporting CFD Model**

366 The CFD modelling approach employed in this study to support observations is documented in detail in Belut et
367 al. (2022). Simulations are conducted using ANSYS FLUENT V.19.3 software. After due examination of the most
368 influent modelling and physical factors affecting the significance of results, a 2D axisymmetric reduction of the
369 inner volume of the SADS is used to perform simulations. A low-Reynolds realizable k- ϵ turbulence model is used
370 to model the incompressible airflow, with a free-inlet boundary condition at the entrance of the SADS, following
371 the guidelines of Belut et al. (2022). Aerosol particle fates are computed through a Lagrangian tracking of their
372 centre of mass, taking into account turbulent dispersion and using a free-inlet boundary condition at the inlet.
373 External forces acting on particles are reduced to drag force, including rarefaction effect. Impaction and
374 interception phenomena are taken into account for wall losses, particles being assumed trapped when hitting a wall
375 (consistent with the liquid nature of present aerosols). An extensive verification of computations with respect to
376 grid size, numerical resolution tolerances and number of used aerosol trajectories was performed, exactly as
377 exposed in Belut et al. (2022). For further insights into the model's design and its applicability to the SADS,
378 interested readers are encouraged to refer to the aforementioned study. Following Belut et al. (2022), simulation
379 results are realistic, within the calculated uncertainties, unless one of the following occurs: 1) the SADS walls are
380 not smooth, 2) there is a difference between the actual and simulated geometry, 3) residual turbulence exists at the
381 SADS inlet (with a Kolmogorov timescale much greater than the aerodynamic response time of the particles, which
382 does not correspond to normal ambient conditions).

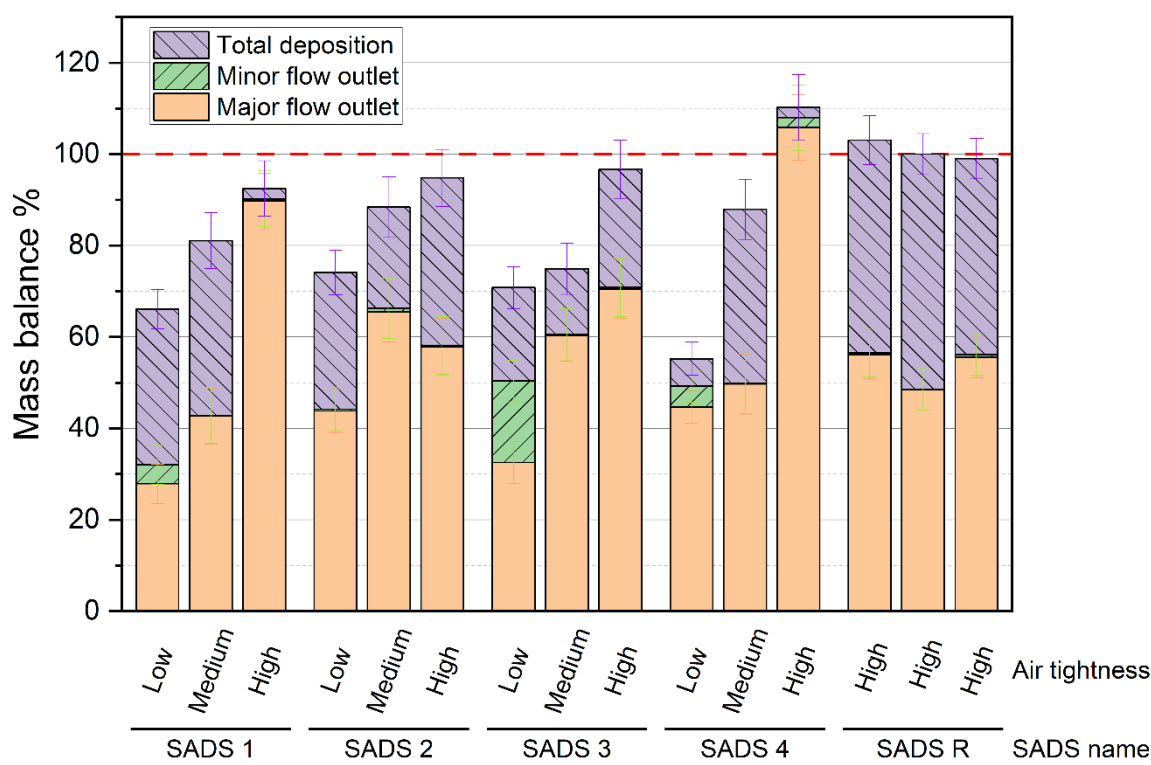
383 **4 Results and discussion**

384 **4.1 Leaks effects**

385 The air tightness tests conducted revealed significant leakages, primarily occurring at the O-ring seal between parts
386 A and B (Figure 2) of the SADS prototypes. Additional leaks were also identified at the connection points between
387 the Open Face Cassette (OFC) and the major and minor outlets of the SADS. Notably, SADS 1, 2, 3, and 4
388 displayed varying levels of air tightness during the tests, with the exception of SADS R, which consistently
389 exhibited high air tightness across all tests. Fig. 6 illustrates the evolution of mass balance and mass distributions
390 for the five SADS prototypes with varying levels of air tightness.

391 The aerosol generated in the three tests was monodisperse with a size distribution centred on a MMAD of
392 $3.11 \pm 0.21 \mu\text{m}$, with a GSD of 1.14 ± 0.03 and a particle number concentration of $10124 \pm 320 \text{ p.c.l.cm}^{-3}$.

393 Tests on the leaks effects on the performance of the SADS were also conducted with aerosols having MMAD of
394 2 and 4.5 μm . The results and conclusions were consistent with the distributions presented, indicating that the
395 outcomes converge towards those presented in the following section.



396 **Figure 6: Mass balance in the SADS prototypes in function of the air tightness level. Error bars represent the**
 397 **standard deviation calculated on five replicates for each condition.**
 398

399 Low air tightness led to a substantial decrease in the mass balance of SADS 1, 2, 3, and 4 (Figure 6), with mass
 400 balances reaching $66 \pm 6.2\%$, $74 \pm 6.8\%$, $70 \pm 6.58\%$, and $55 \pm 7.59\%$, respectively. Only when a high level of
 401 air tightness was achieved could a mass balance of 90 % or higher be attained for all prototypes.

402 Moreover, low air tightness resulted in an undesirable increase in the mass fraction collected at the minor flow
 403 outlet. Presumably, leaks disturbed the airflow in the separation space, leading to the deviation of larger particles
 404 to the minor flow outlet than theoretically expected.

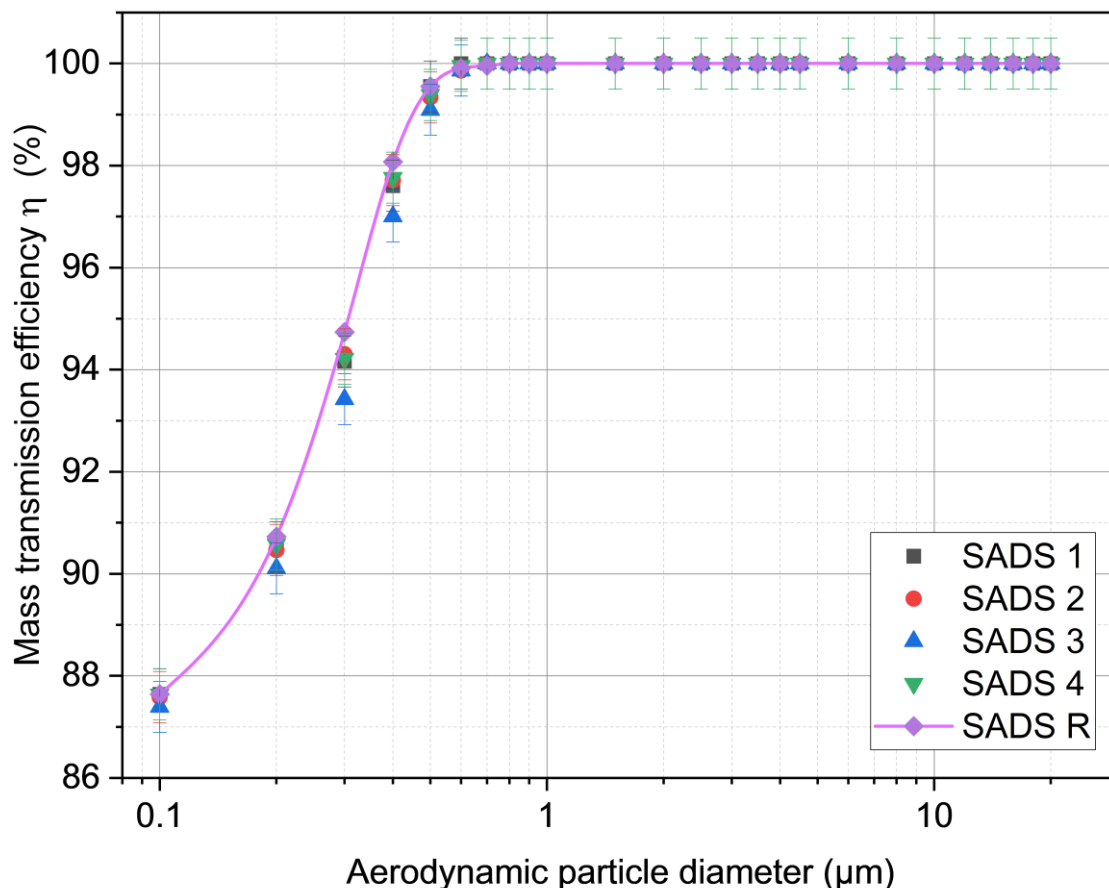
405 Globally, leaks not only influenced the total amount of particles collected within the SADS but also affected the
 406 particles transmission ratio to the major and minor outlets, which make results from leaky SADS unreliable.

407 A systematic leak test is then mandatory before using the SADS for sampling purposes. To ensure reliable and
 408 accurate results, the SADS should only be considered suitable for sampling when the leakage rate (LR) is below 4
 409 $\text{Pa}\cdot\text{s}^{-1}$. Keeping the leakage rate within this acceptable limit will help maintain the integrity of the SADS and
 410 improve the reliability of the data collected during sampling operations. For further development, we also
 411 recommend revising the design of future realization of the SADS to guarantee its air tightness.

412 Due to difficulties in maintaining a constant level of air tightness for SADS 3 and 4 throughout all experimental
 413 tests, further experimentation with these two prototypes was not conducted.

414 **4.2 Theoretical effect of actually manufactured nozzle diameters**

415 Before comparing theoretical and actual performances of manufactured SADS, the effect of the lack of precision
 416 on the actually manufactured nozzle diameters is examined from a theoretical point of view, using the CFD model
 417 with the measured nozzle diameters of SADS 1, 2, 3, 4 and R. The numerical model computed the η_p curves for
 418 each SADS prototype across a range of aerodynamic particle diameters from 0.1 to 20 μm , and the results are
 419 presented in Figure 7. Error bars correspond to one standard deviation of values arising from turbulent dispersion.



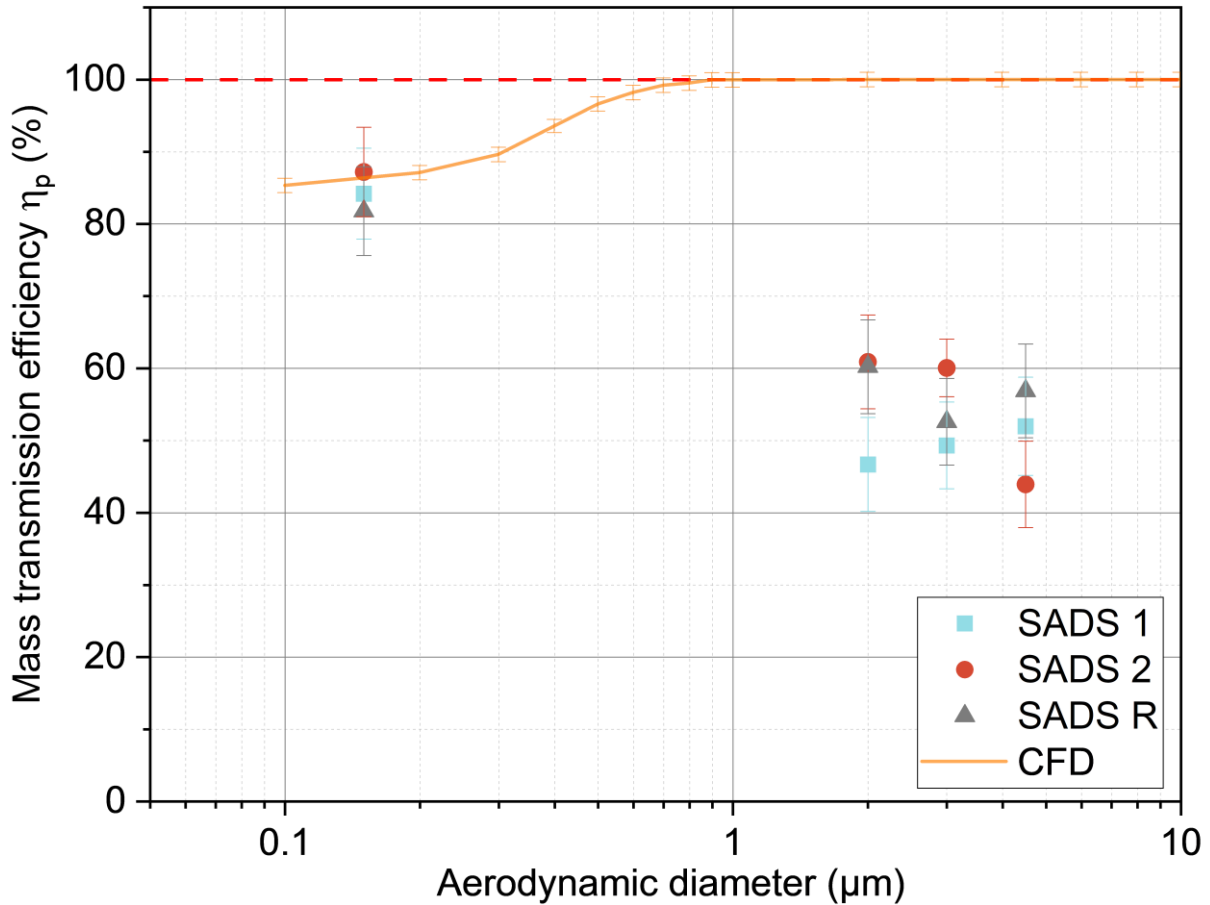
420
 421 Figure 7: Evolution of CFD mass transmission of the SADS prototypes, accounting for variation in nozzles
 422 diameters.

423 The theoretical η_p curves calculated by the numerical model are similar for all SADS prototypes (Figure 7).
 424 SADS 3 exhibits the maximum difference compared to the reference SADS R transmission efficiency curve, but
 425 this difference remains below 3 % for all diameters. Overall, the variations observed in the nozzle diameters
 426 actually machined are not expected to lead to radically different sampling performance between the different
 427 prototypes.

428 These results are consistent with findings from a previous study on a VI by Marple & Chien, 1980a, who observed
 429 that increased ratios between nozzle diameters led to increased wall deposition, above the recommended value of
 430 1.33 (and thus to decreased transmission ratios). From
 431 Table 2, we indeed see that SADS 3 exhibits the largest nozzle diameters ratio (1.39) of the prototypes. All ratios
 432 are, however, below 1.49 as recommended by Marple & Chien, 1980a.

433 **4.3 Actual vs. theoretical particle transmission efficiency**

434 Figure 8 compares the theoretical and actually measured η_p curves of the 3 airtight SADS.



435

436 **Figure 8: Comparison of theoretical CFD transmission efficiency η_p (SADS R) with experimental results for SADS 1,**
 437 **SADS 2, and SADS R. Error bars represent one standard deviation for CFD simulations due to turbulent dispersion**
 438 **and measuring uncertainty for experimental data.**

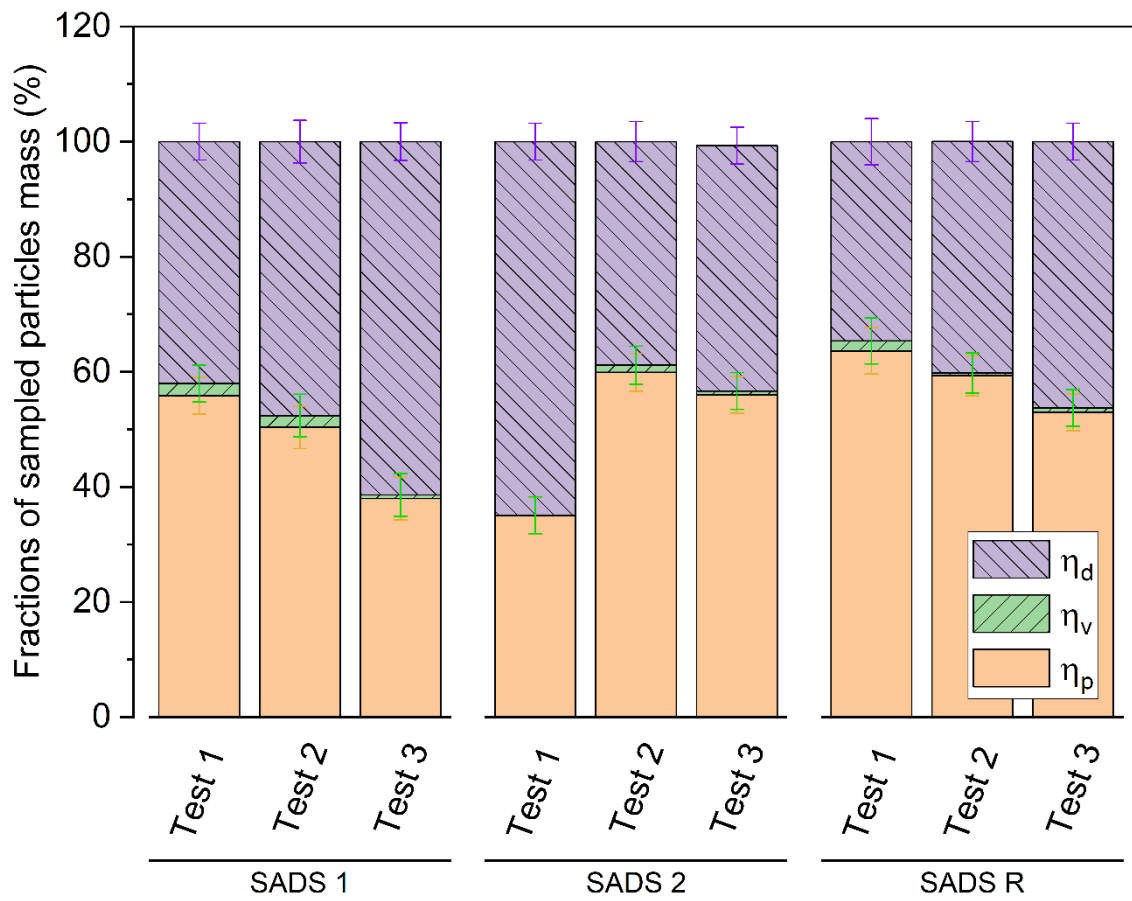
439 For aerosols with a reference diameter of 0.15 μm , numerical predictions are in accordance with experimental
 440 tests, with transmission efficiencies to the major and minor flow outlets close to the ratio between the major and
 441 the minor flow ($\eta_p = 86 \pm 0.58\%$ for the model and $\eta_p = 81.7 \pm 6\%$ experimentally). This corresponds to the
 442 expected behaviour of low inertial particles that are not separated by the SADS. We shall see, however, in the
 443 following section that a substantial fraction of these particles is actually deposited experimentally, in contradiction
 444 with theoretical results.

445 For the inertial particles tested with nominal diameters 2, 3 and 4.5 μm , η_p is measured as always less than about
 446 60 %, whereas 100 % is theoretically expected for the SADS in free-sampling situation. The origin of this
 447 difference is examined first by considering the particles deposition ratio in the next sections.

448 **4.4 Fate of inertial particles and repeatability issues**

449 To illustrate the origin of the unexpectedly low transmission efficiency of inertial particles in the device, the
 450 distribution of all measured η_p , η_v and η_d for 3 repetitions of the experiment and for the 3 airtight prototypes is
 451 shown on Figure 9 and

452 Table 3. Only results for the 4.5 μm particles are shown here for brevity. For these particles, we observe that the
 453 low transmission efficiency η_p is attributable to large ($46.6 \pm 5.4\%$) wall losses (η_d), and not to the misdirection
 454 of particles to the minor outlet. These deposits are not theoretically explained, even if we take into account the
 455 lack of precision of machined nozzle diameters (Figure 8), and we can note that they apparently vary randomly
 456 across repetitions with a large coefficient of variation for η_d (22.1%). These variations are then likely to be
 457 attributable to the assembly process of the SADS, since other influencing parameters were monitored and
 458 controlled (flow rates, aerosol particle sizes, homogeneity of concentrations in the BOA, SADS leakage rate,
 459 similarity of sampled masses).



460
 461 **Figure 9: Distribution of the fate of inertial particles with a reference diameter of 4.5 μm in multiple repetitions, for**
 462 **SADS 1, SADS 2, and SADS R at High Airtightness Level. Error bars represent the measuring uncertainty associated**
 463 **with the data points."**

464

465 **Table 3: Transmission ratio to the major and minor outlets and deposition ratio for SADS 1, 2 and R.**

SADS name	Tests	η_p [%]	η_v [%]	η_d [%]
SADS 1	Test 1	55.9	2.08	42.1
	Test 2	50.3	2.04	47.6
	Test 3	38.0	1.26	61.4
	Average	48.1	1.79	50.4
	SD	9.2	0.46	10.0
SADS 2	Test 1	35.0	0.07	64.9
	Test 2	59.9	1.26	38.9
	Test 3	56.0	0.64	43.4
	Average	50.3	0.66	49.0
	SD	13.4	0.60	13.9
SADS R	Test 1	63.6	1.73	34.6
	Test 2	59.3	0.48	40.2
	Test 3	53.0	0.75	46.3
	Average	58.6	0.99	40.4
	SD	5.4	0.66	5.8
Total Average		52.3	1.15	46.6
SD		5.6	0.58	5.4

466 **4.5 Detailed particles fate measured for SADS-R**

467 Figure 10(a) and Figure 10(b) present images depicting a typical deposition that occurs inside the SADS after the
 468 sampling process. Notably, a significant amount of liquid particles can be seen on the external walls of the nozzles.
 469 Deposits can also be found on the internal walls of the nozzles, but they are difficult to capture in photographs.
 470 Additionally, in certain tests, projections of macroscopic droplets from the nozzles to the walls of the plenum were
 471 also observed.



(a) acceleration nozzle (b) Collection nozzle

474 **Figure 10: Pictures of particles deposition outside the nozzle.**

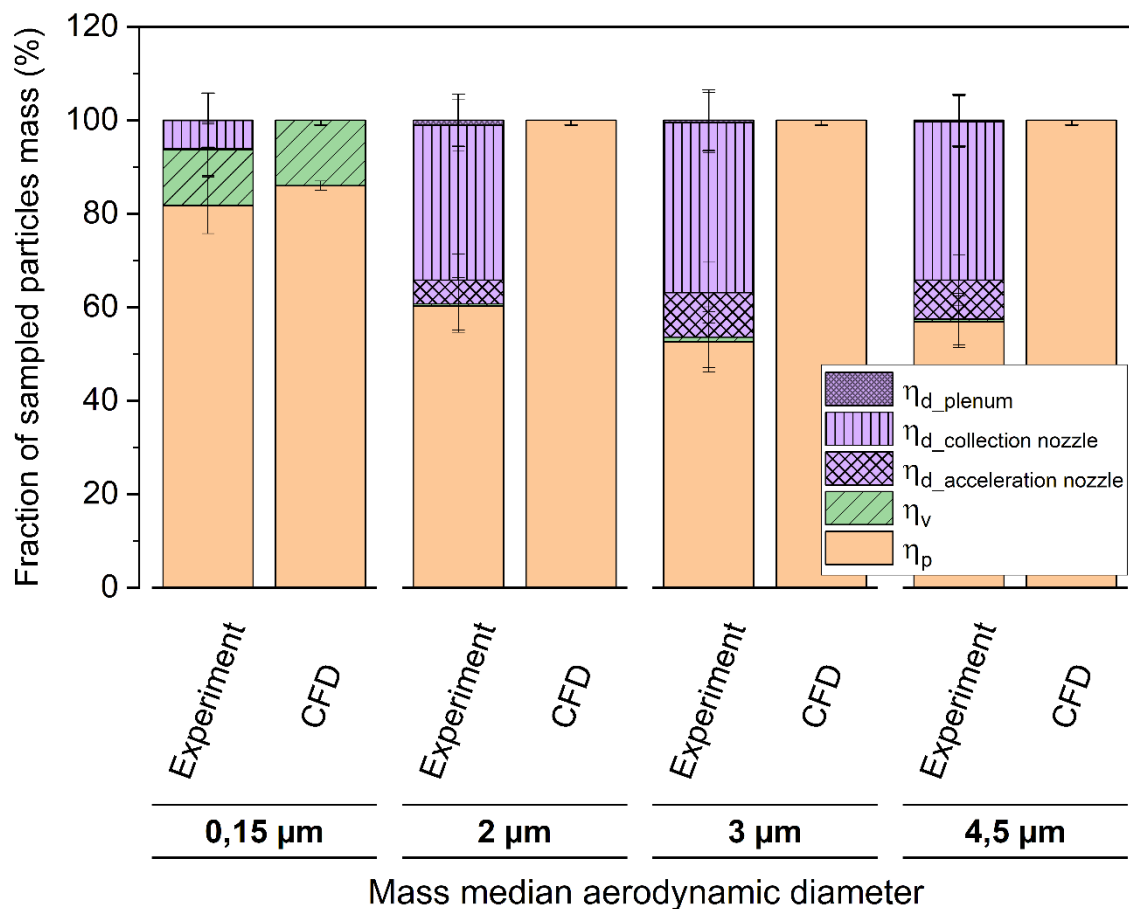
475 To better understand the localization and underlying reasons for particle deposition in the SADS, independently
 476 of variations between prototypes, the detailed transmission ratios and position-resolved deposition ratios for the
 477 reference SADS-R are given on

478 Figure 11, for all tested particle sizes. Values are averaged over 3 repetitions.

479 For particles with reference diameter $0.15 \mu\text{m}$, wall deposition is primarily located on the collection nozzle, with
 480 $6 \pm 5.8 \%$ of sampled mass, though it should be almost zero theoretically ($0.44 \pm 0.58 \%$).

481 For particles with reference diameters 2, 3 and $4.5 \mu\text{m}$, the experimental results show substantial particle
 482 depositions (43 % of sampled mass in average), unpredicted by theory either ($0.2 \pm 0.1 \%$). These experimental
 483 wall deposits seem almost independent of particle diameter for these inertial particles. The distribution of deposits

484 across zones reveals that the majority of particles deposit on the collection nozzle ($34.5 \pm 3.4 \%$), followed by the
 485 acceleration nozzle ($7.6 \pm 3.4 \%$), with minimal deposition in the plenum ($0.6 \pm 3.4 \%$).



486
 487 **Figure 11: Mass distribution in SADS R exposed to four different particle size distributions: experimental and**
 488 **numerical study for precise wall deposition localization and transmission efficiency analysis. (Three repetitions, error**
 489 **bars represent measuring uncertainty). It is essential to note that most of the deposits observed can contaminate the**
 490 **vapour phase measurements at the minor outlet if particles evaporate after deposition. Indeed, wall deposition on the**
 491 **acceleration nozzle is located before separation, and most of the deposit of the collection nozzle is actually located on its**
 492 **outside walls (fraction of the deposit which is visible to the unaided eye).**

493 Having ruled out the effects of leakage and machining inaccuracies in nozzle diameter, we can envisage several
 494 reasons for these deposits, which are not predicted by the numerical model. Firstly, the simulated geometry may
 495 not correspond to the real geometry for aspects other than nozzle diameter. In particular, the variations in deposits
 496 between the tests (Figure 9 and
 497 Figure 11) suggest variability in the assembly of the 2 parts of the SADS in relation to each other, and therefore a
 498 geometry of the interior domain of the SADS that is not only variable but also different from what is simulated.
 499 These variations may correspond in particular to a misalignment of the nozzles with respect to each other, which
 500 can easily explain the impaction of inertial particles outside the collection nozzle (Loo & Cork, 1988). In the
 501 following section, the sensitivity of SADS performances with respect to nozzle misalignment is thus illustrated
 502 theoretically.

503 4.6 Theoretical effect of nozzle misalignment

504 Study by Loo & Cork (1988) emphasized the importance of maintaining axial alignment between the acceleration
 505 and collection nozzle of a VI. In their case, which is very different from the SADS in terms of dimensions and air

506 flow rates, they recommend avoiding an offset of more than 1.6 % of nozzle diameter and observe that each 1.6 %
507 increase in misalignment leads to a 1 % increase in nozzle wall loss. Meeting this criterion in the case of the SADS
508 would mean avoiding a misalignment of more than 0.013 mm, which is challenging from a mechanical design
509 point of view. Experimentally, measuring the misalignment offset of the mounted SADS was not feasible.
510 However, a sensitivity analysis can be performed by means of parametric CFD computations to explore the impact
511 of this parameter.

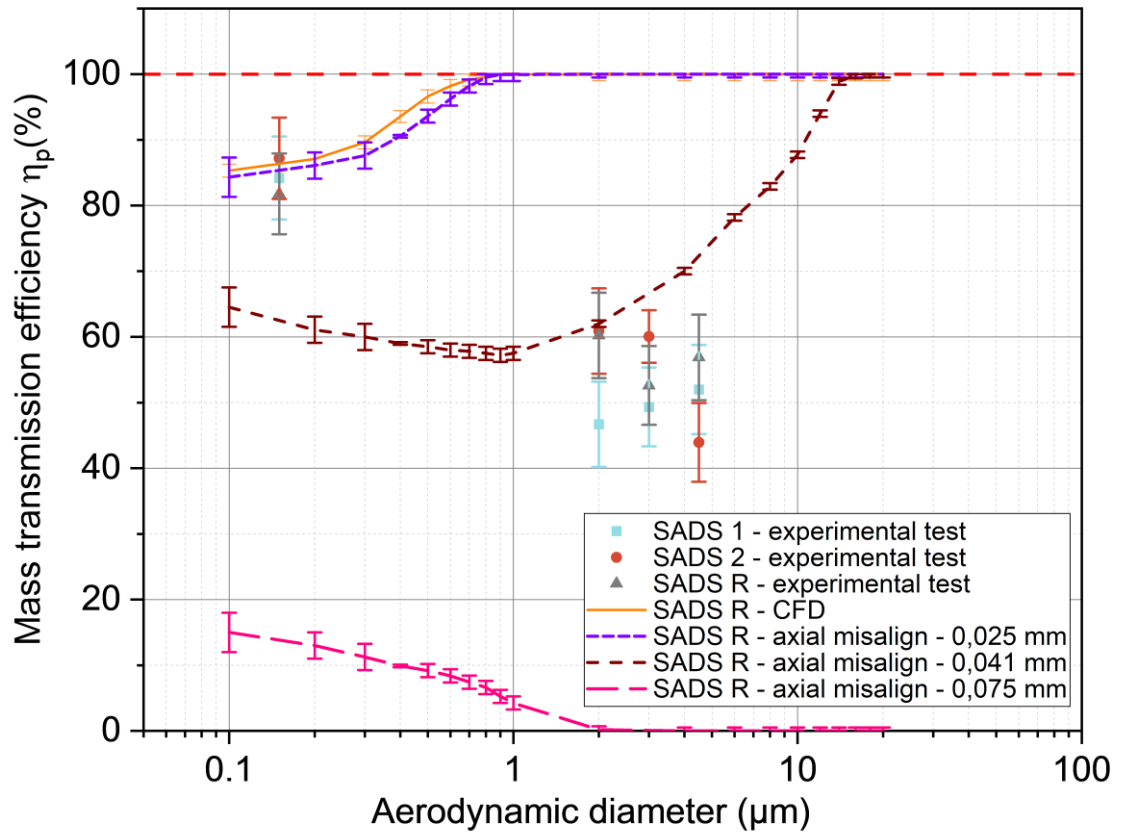
512

513 Simulations were hence carried out with relative displacements of the collection nozzle with respect to the
514 acceleration nozzle (Figure 2) in the Z-axis direction, with likely values of the axial backlash between the two
515 parts of the SADS. These parts are assembled by manually fitting together a shaft and a 37 mm diameter hole.
516 Following ISO system of limits and fits, this corresponds to a H7/h6 clearance fit (location fit), whence a possible
517 axial backlash in the range 0 to 0.041 mm is deduced. Parametric computations were then performed for axial
518 backlashes of 0, 0.025 and 0.041 mm respectively (corresponding to 0, 3.1 % and 5.1 % of the nozzle diameter
519 respectively). A simulation with an extreme backlash of 0.075 mm (9.4 % of nozzle diameter) was also performed
520 for information, which could correspond to a more tolerant H8/f7 ISO clearance fit (close-running fit).

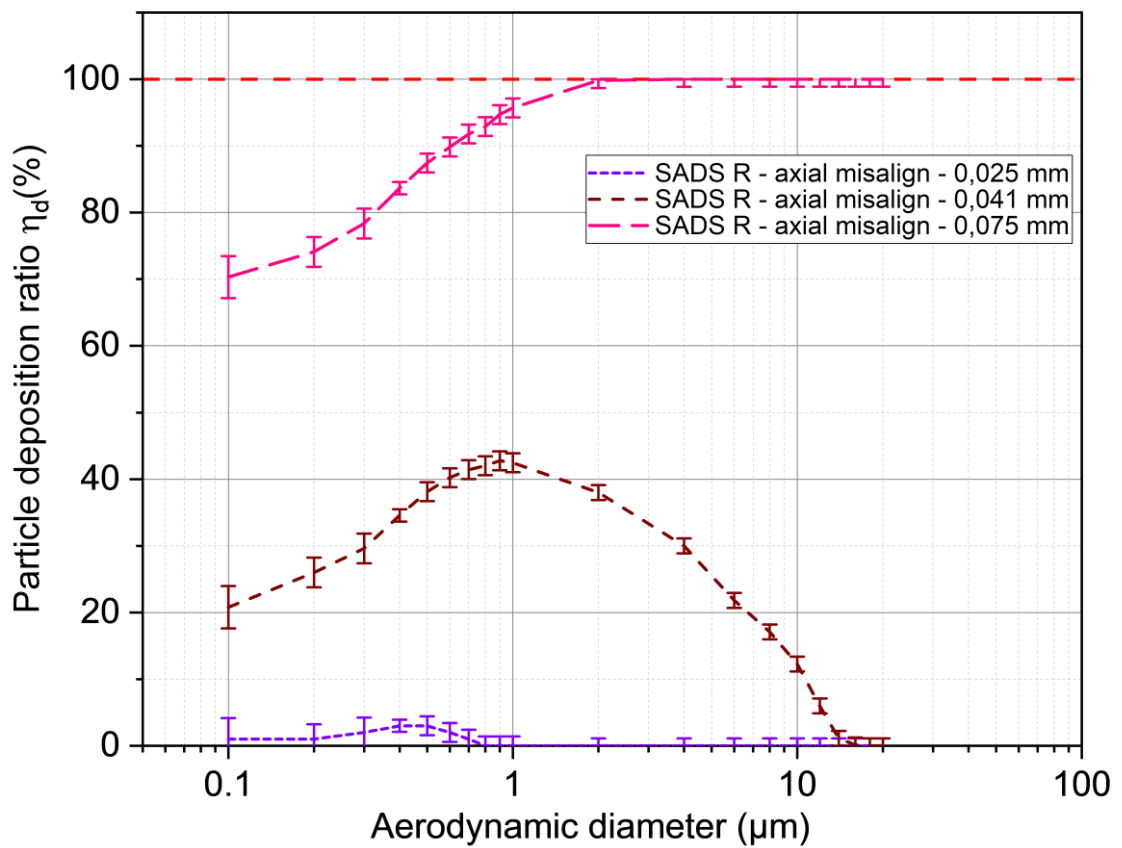
521 Figure 12 displays the corresponding numerical simulation results for the transmission efficiency and wall
522 deposition, compared with experimental measurements of SADS 1, 2, and R, illustrating the possible effect of
523 axial misalignment on η_p .

524

525



526 A)



527 B)

528 **Figure 12: Misalignment effect on mass transmission efficiency (A) and Particle deposition ratio (B), evaluated by**
 529 **numerical simulations and experimental tests.**

530 Results show that likely values of the axial mechanical backlash between the two parts lead to a severe decrease
531 of η_p due to dramatically increasing wall losses η_d on the collection nozzle external walls, especially for the most
532 inertial particles. This finding is compatible with experimental measurements. Axial misalignment of the device
533 is therefore a possible cause of the differences in performance between the ideal version and the mechanical
534 realization of the SADS, for the most inertial particles tested. Of course, present simulations can only qualitatively
535 reproduce the tendency of the experiment, since they were not performed with the actual axial backlash which is
536 unknown and which varies between each SADS assembly. Also, the effects of other existing mechanical
537 backlashes were not numerically tested and necessarily contribute to sampling performances (tolerance on the
538 separation length between nozzles, existing angle between the axes of the two parts of the SADS, etc.).
539 Based on the analysis of the results, we can conclude that the maximum allowable misalignment during the
540 assembly of the SADS, between the collection nozzle and the acceleration nozzle, is established at 0.025 mm, as
541 evidenced by the violet curve. Notably, this curve consistently aligns with that of the SADS R-CFD, representing
542 a curve with perfect alignment.

543 **5 Conclusion and discussion**

544 This study experimentally evaluated the dichotomous sampling performance (gas and particles) of 5 SADS
545 prototypes (2009 version) of identical design, and for an aerosol of liquid particles with aerodynamic diameters of
546 0.15, 2, 3 and 4.5 μm . The study was carried out for constant air flows set in accordance with SADS specifications.
547 Lab tests were carried out in a dedicated controlled generation environment, the BOA, in which monodisperse
548 aerosols marked with a fluorescent dye were emitted, thanks to the modification of the CMAG generator to
549 accommodate the use of glycerol and fluorescein as condensing vapour and nuclei respectively.
550 SADS sampling performance in terms of total mass sampled, particle fraction transmitted to the major outlet and
551 particle losses at the walls were put into perspective with the details of mechanical construction and with the
552 operating conditions of the prototypes: leak rate, repeatability between successive assemblies, imprecision of
553 machined nozzles diameters, and axial misalignment of the assembly.
554 The measured sampling performances were compared to their theoretical counterparts computed by CFD in Belut
555 et al. (2022), and CFD was also used to study the theoretical effect of variations in the geometry of machined
556 SADS relative to the plans, regarding the nozzles diameters and nozzle misalignments.
557 With the originally proposed design, the SADS assembly was found easily leaky, but consequences on sampling
558 could be overcome when a prior leak test with leakage rate LR below 4 Pa.s⁻¹ was passed.
559 Sampling performances were found little reproducible during successive SADS assemblies (between tests,
560 CV=22.1 % for wall losses). Theoretically unpredicted large (40-46 % of sampled mass) wall losses were
561 measured for particles larger than 2 μm , located mostly (80 %) on the external walls of the collection nozzle.
562 Assembly repeatability issues and simulations of SADS parts misalignment effect by CFD suggest that these
563 undesirable particle deposits are due to the mechanical backlashes of the assembly, and not to the imprecision of
564 actually machined nozzles diameters. Indeed, the measured variation of nozzle diameters in the range (-4.5 %,
565 +3.7 %) with respect to nominal values were found to theoretically affect marginally (<3 %) aerosol transmission
566 efficiencies.
567 Present results suggest that although the dichotomous sampling performances of the SADS are theoretically
568 interesting for workplace exposure assessment to SVOC aerosols, its actual realization fails in reaching theoretical

569 performances for micron-sized particles, due to mechanical design issues. Airtightness, nozzle alignment and
 570 repeatability of assembly are not sufficiently guaranteed by its initial design and future development should focus
 571 on improving these aspects to obtain a sampler suitable for field studies.

572 However, several biases may have affected the findings of the study. For example, rare macroscopic particles are
 573 sometimes emitted by the CMAG and may have been sampled by the SADS, biasing the separation performance
 574 measurements and especially the deposition measurements. However, we believe that this possibility is largely
 575 controlled by the real-time monitoring of particle sizes in the test rig, and by the simultaneous use of several SADS
 576 in the test rig. Regarding the plausibility of the simulation results, it is, of course, limited by the physical
 577 phenomena actually taken into account. Calculation errors are limited by the verification procedure used (Belut et
 578 al., 2022), which guarantees a numerical error of less than 0.5 % on the particulate fractions deposited and
 579 transmitted. However, actual variations in the geometry of assembled SADS compared with the drawings (due to
 580 machining inaccuracies other than nozzle diameters) are not taken into account, nor is wall roughness, despite its
 581 acknowledged effect on deposits. The roughness of the machined acceleration nozzles could therefore help to
 582 explain the deposition of particles in this nozzle, which are not predicted by calculations that assume a perfectly
 583 smooth nozzle. Similarly, the more or less pronounced sharpness of the sampling orifice actually machined can
 584 have a significant influence on the inlet particle velocity and concentration profile, and therefore on the actual
 585 performance of the SADS (Belut et al., 2022).

586 Nevertheless, the lack of repeatability of SADS performance between successive assemblies, its low and variable
 587 airtightness level and its radial clearance large enough to cause a significant misalignment of the nozzles (typically
 588 5 %) have sufficiently important effects for these possible limitations of the study not to call into question its
 589 conclusions.

590 Overall, these results clearly show that it is mechanically difficult to design a SADS that meets the theoretical
 591 specifications. In fact, the alignment tolerances require precise machining, which may be an obstacle to the
 592 development of this device. It should be added that the head losses of the device at its nominal flow rate are
 593 1400 Pa on the major flow side and 3700 Pa on the minor flow side (Belut et al., 2022). These head losses are at
 594 the limit of the performance of individual sampling pumps, especially when considering the additional head losses
 595 caused by the collection media downstream of the SADS outlets. This raises the question of whether the device
 596 should be completely redesigned, with larger nozzle diameters that are easier to align mechanically and generate
 597 less pressure drop.

598 By addressing the identified challenges and incorporating further refinements in the SADS design and operation,
 599 researchers can enhance its reliability, accuracy, and applicability in various aerosol sampling applications,
 600 contributing to advancements in aerosol science and related fields.

601 7 Table of Symbols

Greek Letters		
Δt	Duration of the leak test	(s)
η_p	particles transmission efficiency to the particle outlet (major flow)	(-)

η_v	particles transmission efficiency to the vapour outlet (minor flow)	(-)
η_d	particles deposition ratio	(-)
$\eta_{d_a}, \eta_{d_c}, \eta_{d_p}$	particles deposition ratio in the acceleration nozzle, collection nozzle and in the plenum respectively	(-)
μ	Air viscosity	Pa.s ⁻¹
ρ	Air density	kg.m ⁻³
ρ_0	Reference particle density, equals to 1000 kg.m ⁻³	(kg.m ⁻³)
ρ_p	Relative particle density	(kg.m ⁻³)
x	Shape factor	(-)
Lowercase Latin letters		
d_{ae}	Aerodynamic diameter	(μ m)
d_m	Electrical mobility diameter	(μ m)
d_{ev}	Equivalent volume diameter	
m_{CFC}	Mass of particles collected inside a close-face cassette	(ng)
m_{dep_a}	Mass of particles collected on the acceleration nozzle walls of the SADS	(ng)
m_{dep_c}	Mass of particles collected on the collection nozzle walls of the SADS	(ng)
m_{dep_p}	Mass of particles collected on the plenum walls of the SADS	(ng)
m_{inlet}	Mass of sampled particles at the inlet	(ng)
m_{major}	Mass of particles collected at the major flow outlet	(ng)
m_{minor}	Mass of particles collected at the minor flow outlet	(ng)
Uppercase Latin letters (Variables)		
Cu	the Cunningham slip correction factor	(-)
GSD	Geometric standard deviation	(-)
LLOQ	Lower limit of quantification	(ng.L ⁻¹)
LR	Leakage rate	(Pa.s ⁻¹)
Mb_{SADS}	Mass balance of SADS	(-)
MMAD	Mass median aerodynamic diameter	(μ m)
P	Pressure	(Pa)
P_0 and P_f	Pressures inside a SADS at T=0 and T=final time, during the leak test.	(Pa)
T	Temperature	(°C)
ULOQ	Upper limit of quantification	(ng.L ⁻¹)
V_p	Particle volume	(μ m ³)
Abbreviations		

APS	Aerodynamic Particle Sizer	
BOA	Bench of Organic Aerosol	
CFC	Close-Face cassette	
CMAG	Condensation Monodisperse Aerosol Generator	
FMPS	Fast Mobility Particle Sizer	
OFC	Open-Face cassette	
SADS	Semivolatile Aerosol Dichotomous Sampler	
SEM	Scanning Electron Microscopy	
WD	Wall depositions	

602 **8. Author contribution**

603 BS, EB, EG and RO conceptualized the research project. NR, BS and EB developed the methodology and NR was
604 responsible of the investigation. BS and EB validated the results. EG was responsible for the supervision of the
605 project. NR wrote the original draft preparation and BS, EB and EG reviewed and edited the manuscript.

606 **9. Competing interests**

607 The authors declare that they have no conflict of interest.

608 **10. Financial support**

609 This research did not receive any specific grant from funding agencies in the public, commercial, or not-for-profit
610 sectors.

611 **8 Bibliography**

612 Belut, E., Rekeb, N., Sutter, B., and Géhin, E.: Revisiting the CFD modeling of a virtual impactor with inverted
613 split ratio: Highlighting some determinants of representativeness, *J. Aerosol Sci.*, 166, 106068,
614 <https://doi.org/10.1016/j.jaerosci.2022.106068>, 2022.

615 Cooper, S. J., Raynor, P. C., and Leith, D.: Evaporation of Mineral Oil in a Mist Collector, *Appl. Occup. Environ.*
616 *Hyg.*, 11, 1204–1211, <https://doi.org/10.1080/1047322X.1996.10389398>, 1996.

617 Kim, S. W. and Raynor, P. C.: A New Semivolatile Aerosol Dichotomous Sampler, *Ann. Occup. Hyg.*, 53, 239–
618 248, <https://doi.org/10.1093/annhyg/mep008>, 2009.

619 Kim, S. W. and Raynor, P. C.: Experimental Evaluation of Oil Mists Using a Semivolatile Aerosol Dichotomous
620 Sampler, *J. Occup. Environ. Hyg.*, 7, 203–215, <https://doi.org/10.1080/15459620903582244>, 2010a.

621 Kim, S. W. and Raynor, P. C.: Optimization of the Design of a Semivolatile Aerosol Dichotomous Sampler,
622 *Aerosol Sci. Technol.*, 44, 129–140, <https://doi.org/10.1080/02786820903426739>, 2010b.

623 Kim, S. W., Lee, E. G., Lee, T., Lee, L. A., and Harper, M.: Exposure to chlorpyrifos in gaseous and particulate
624 form in greenhouses: a pilot study, *J. Occup. Environ. Hyg.*, 11, 547–555, 2014.

625 Leith, D., Leith, F. A., and Boundy, M. G.: Laboratory Measurements of Oil Mist Concentrations Using Filters
626 and an Electrostatic Precipitator, *Am. Ind. Hyg. Assoc. J.*, <https://doi.org/10.1080/15428119691014242>, 2010.

- 627 Lillienberg, L., Burdorf, A., Mathiasson, L., and Thörneby, L.: Exposure to Metalworking Fluid Aerosols and
628 Determinants of Exposure, *Ann. Occup. Hyg.*, 52, 597–605, <https://doi.org/10.1093/annhyg/men043>, 2008.
- 629 Loo, B. W. and Cork, C. P.: Development of High Efficiency Virtual Impactors, *Aerosol Sci. Technol.*, 9, 167–
630 176, <https://doi.org/10.1080/02786828808959205>, 1988.
- 631 Marple, V. A. and Chien, C. M.: Virtual Impactors: A Theoretical Study, *Environ. Sci. Technol.*, 14, 976–985,
632 <https://doi.org/10.1021/es60168a019>, 1980.
- 633 Olsen, R., Thomassen, Y., Koch, W., Halgard, K., Bakke, B., and Ellingsen, D. G.: Performance testing of a
634 personal sampler for full-shift sampling of oil mist and oil vapour, STAMI National Institute of Occupational
635 Health, 2013.
- 636 Park, D., Stewart, P. a, and Coble, J. B.: Determinants of Exposure to Metalworking Fluid Aerosols: A Literature
637 Review and Analysis of Reported Measurements, *Ann. Occup. Hyg.*, 53, 271–288,
638 <https://doi.org/10.1093/annhyg/mep005>, 2009.
- 639 Park, S. S., Kang, M. S., and Hwang, J.: Oil mist collection and oil mist-to-gas conversion via dielectric barrier
640 discharge at atmospheric pressure, *Sep. Purif. Technol.*, 151, 324–331,
641 <https://doi.org/10.1016/j.seppur.2015.07.059>, 2015.
- 642 Raffy, G., Mercier, F., Glorennec, P., Mandin, C., and Le Bot, B.: Oral bioaccessibility of semi-volatile organic
643 compounds (SVOCs) in settled dust: A review of measurement methods, data and influencing factors, *J. Hazard.
644 Mater.*, 352, 215–227, <https://doi.org/10.1016/j.jhazmat.2018.03.035>, 2018.
- 645 Raynor, P. C. and Leith, D.: Evaporation of accumulated multicomponent liquids from fibrous filters, *Ann. Occup.
646 Hyg.*, 43, 181–192, <https://doi.org/10.1093/annhyg/43.3.181>, 1999.
- 647 Raynor, P. C., Volckens, J., and Leith, D.: Modeling Evaporative Loss of Oil Mist Collected by Sampling Filters,
648 *Appl. Occup. Environ. Hyg.*, 15, 90–96, <https://doi.org/10.1080/104732200301890>, 2000.
- 649 Roberts, J. W., Wallace, L. A., Camann, D. E., Dickey, P., Gilbert, S. G., Lewis, R. G., and Takaro, T. K.:
650 Monitoring and Reducing Exposure of Infants to Pollutants in House Dust, in: *Reviews of Environmental
651 Contamination and Toxicology Vol 201*, edited by: Whitacre, D. M., Springer US, Boston, MA, 1–39, 2009.
- 652 Simpson, A. T.: Comparison of Methods for the Measurement of Mist and Vapor from Light Mineral Oil–Based
653 Metalworking Fluids, *Appl. Occup. Environ. Hyg.*, 18, 865–876, <https://doi.org/10.1080/10473220390237386>,
654 2003.
- 655 Simpson, A. T., Groves, J. A., Unwin, J., and Piney, M.: Mineral oil metal working fluids (MWFs)—development
656 of practical criteria for mist sampling, *Ann. Occup. Hyg.*, 44, 165–172, <https://doi.org/10.1093/annhyg/44.3.165>,
657 2000.
- 658 Sinclair, David. and La Mer, V. K.: Light Scattering as a Measure of Particle Size in Aerosols. The Production of
659 Monodisperse Aerosols., *Chem. Rev.*, 44, 245–267, <https://doi.org/10.1021/cr60138a001>, 1949.
- 660 Steiner, S., Majeed, S., Kratzer, G., Hoeng, J., and Frentzel, S.: A new fluorescence-based method for
661 characterizing *in vitro* aerosol exposure systems, *Toxicol. In Vitro*, 38, 150–158,
662 <https://doi.org/10.1016/j.tiv.2016.09.018>, 2017.
- 663 Sutter, B., Bémer, D., Appert-Collin, J.-C., Thomas, D., and Midoux, N.: Evaporation of Liquid Semi-Volatile
664 Aerosols Collected on Fibrous Filters, *Aerosol Sci. Technol.*, 44, 395–404,
665 <https://doi.org/10.1080/02786821003674244>, 2010.
- 666 Technical Overview of Volatile Organic Compounds: [https://www.epa.gov/indoor-air-quality-iaq/technical-](https://www.epa.gov/indoor-air-quality-iaq/technical-overview-volatile-organic-compounds)
667 [overview-volatile-organic-compounds](https://www.epa.gov/indoor-air-quality-iaq/technical-overview-volatile-organic-compounds), last access: 5 February 2020.
- 668 Volckens, J.: Partitioning Theory for Respiratory Deposition of Semivolatile Aerosols, *Ann. Occup. Hyg.*, 47,
669 157–164, <https://doi.org/10.1093/annhyg/meg015>, 2003.

670 Volckens, J., Boundy, M., Leith, D., and Hands, D.: Oil Mist Concentration: A Comparison of Sampling Methods,
671 Am. Ind. Hyg. Assoc. J., <https://doi.org/10.1080/00028899908984492>, 2010.

672 Wlaschitz, P. and Höflinger, W.: A new measuring method to detect the emissions of metal working fluid mist, J.
673 Hazard. Mater., 144, 736–741, <https://doi.org/10.1016/j.jhazmat.2007.01.104>, 2007.

674